Entanglement and coherence in photoionization of H_2 by an ultrashort XUV laser pulse

Takanori Nishi, Erik Lötstedt, and Kaoru Yamanouchi*
Department of Chemistry, School of Science, The University of Tokyo, 7-3-1 Hongo, Bunkyo-ku, Tokyo 113-0033, Japan

(Received 15 April 2019; published 30 July 2019)

We make a theoretical investigation of photoionization of an H_2 molecule, induced by the irradiation of an ultrashort extreme ultraviolet (XUV) laser pulse. We consider a system composed of a photoelectron ejected from H_2 and the resultant H_2^+ as a bipartite system. In order to clarify how the interparticle correlations among two electrons and two protons in H_2 are reflected to the bipartite system, we examine the entanglement between the photoelectron and the vibrational states of H_2^+ as well as the coherence in the vibrational states of H_2^+ by simulating the photoionization process of one-dimensional H_2. In the simulation, we solve a time-dependent Schrödinger equation using a symmetry-adapted grid method. On the basis of the simulations with ten different sets of three parameters characterizing an ultrashort XUV laser pulse, i.e., the pulse duration, the wavelength, and the peak intensity, we show that the extent of the entanglement depends sensitively on the coherence in the vibrational states of H_2^+.

DOI: 10.1103/PhysRevA.100.013421

I. INTRODUCTION

Properties of atomic and molecular systems composed of particles such as electrons and nuclei are characterized by the correlations among the constituent particles. For example, the configuration interaction in quantum chemical calculations [1] and the correlation energy functional in the density functional theory [2] originate from the electron-electron correlation, and the nonadiabatic transitions among potential energy surfaces of molecules [3,4] originate from the electron-nuclear correlation.

In recent years, the interparticle correlation in atoms and molecules has been related to entanglement [5], which was originally introduced by Schrödinger [6]. Especially, the entanglement in a bipartite system, which has been investigated intensively in quantum information science during the past three decades [7–11], is now being introduced into atomic and molecular science to explore the interparticle correlation.

Using entanglement, we can quantify the correlation between two degrees of freedom in a bipartite system. Indeed, the correlation between an electron and a proton in the ground state of a hydrogen atom was investigated in terms of entanglement [12] by the density matrix formalism developed in quantum information theory [13]. For a hydrogen atom, the entanglement in one-photon ionization [14] and that in strong-field ionization [15] were investigated. Entanglement was also used for characterizing the correlation in molecular systems. It was shown that the electron-electron correlation in an H_2 molecule, quantified using entanglement as a function of internuclear distance, exhibits a different behavior from the correlation energy, which is supposed to represent the extent of the electron-electron correlation [16,17]. The correlation between the electronic and the vibrational degrees of freedom in molecules is also evaluated by using entanglement [18–20]. The intramolecular vibrational energy redistribution in H_2O originating from the correlation between the vibrational modes was also discussed in terms of entanglement [21].

On the other hand, the property called coherence has also been used in describing correlation in atomic and molecular systems. The recent development of subfemtosecond laser pulses has enabled us to create a highly coherent superposition of electronic states of rare gas atom ions [22]. For example, a method of controlling the coherence in two-level atomic ions created by ionization of Ne and Xe with an intense IR pulse was proposed theoretically [23] and such control of the coherence was demonstrated by transient absorption spectroscopy of Kr, which is ionized by an intense few-cycle near-IR pulse and probed by a XUV pulse whose duration is 150 as [22]. More recently, it was revealed theoretically that the extent of coherence in a two-level atomic ion can be enhanced when the bandwidth of the XUV pulse inducing photoionization becomes comparable with the energy separation between the two levels or when the XUV pulse is composed of two colors whose frequency difference is the same as the energy separation between the two levels of the atomic ion [24].

Considering that both of the two properties, i.e., entanglement and coherence, represent the correlation among the constituent particles of the system, it would be meaningful to clarify the difference between these two properties. The best system with which we could learn how entanglement and coherence are related to each other is a bipartite system because entanglement is a property of the total system while coherence is a property of each of the subsystems. In a recent theoretical study on the excitation of Cs_2 by a sequence of chirped laser pulses, it was shown that the time evolution of the entanglement between the electronic part and the vibrational part of the vibronic wave packet can be characterized by the coherence in the electronic part [25,26].

In the present study, we investigate theoretically the photoionization of H_2 creating a bipartite system composed of

*kaoru@chem.s.u-tokyo.ac.jp

an entangled pair of a photoelectron and an H_2^+ ion together with a coherent superposition of the vibrational states of H_2^+. We solve the time-dependent Schrödinger equation (TDSE) numerically for photoionization of H_2, and evaluate the degree of the entanglement between a photoelectron and H_2^+ as well as the coherence in the vibrational states of H_2^+, and examine how the entanglement and the coherence describe the interparticle correlations in the system differently. We also show how the entanglement and the coherence vary depending on the laser parameters such as the wavelength, the peak intensity, and the pulse duration of the ionization laser pulse. Finally, we propose an experimental pump-probe scheme by which we can extract the entanglement and the coherence in photoionization of a molecular system. Throughout the present paper, atomic units (a.u.) are used unless otherwise indicated.

II. THEORY

A. Entanglement and coherence

We consider a system composed of a photoelectron and H_2^+ prepared in the electronic ground state, which are produced from one-dimensional H_2 in the electronic and vibrational ground state upon photoionization. We assume that two protons and two electrons move along the one-dimensional axis in response to a laser pulse whose polarization is along this axis. Then, as long as we assume that the electron spin state is singlet, a wave function of the composite system of $H_2^+ + e^-$ is written as

$$|\Psi\rangle = \sum_{hlk} c_{hlk}|\zeta_h\rangle \otimes \frac{1}{2}\mathcal{A}\{|\eta_l,\alpha\rangle_1 \otimes |\phi_k,\beta\rangle_2 - |\eta_l,\beta\rangle_1 \otimes |\phi_k,\alpha\rangle_2\}, \tag{1}$$

where $|\zeta_h\rangle$ is the basis for the nuclear vibration, $|\eta_l\rangle$ is the basis for the bound electron in H_2^+, $|\phi_k\rangle$ is the basis for the photoelectron interacting with the H_2^+ ionic core, α and β are the spin functions, and $\mathcal{A}$ is the antisymmetrizer of the spatial and the spin coordinates. The antisymmetrizer is defined using the identity operator I_{12} and the exchange operator E_{12} as $\mathcal{A} = I_{12} - E_{12}$, which exchanges the spatial and the spin coordinates of two electrons.

In general, when two distinguishable particles are described by a product state, $|\varphi\rangle_1|\chi\rangle_2$, two particles are regarded as nonentangled, while they are regarded as entangled when no product state can be assigned to them. When the system is composed of indistinguishable particles, the same entanglement criteria used for distinguishable particles cannot be applied. Various entanglement criteria for the system of indistinguishable particles have been proposed [27–30], but these criteria have been developed for the system composed of one kind of indistinguishable particle, e.g., the system composed of electrons exclusively. In contrast, the system we treat is composed of two kinds of indistinguishable particles, i.e., two electrons and two protons. When the indistinguishable particles are spatially separated so that they can be measured separately, the indistinguishable particles can be treated as distinguishable particles [31] and the measure of entanglement, which has been developed in the investigation of distinguishable particles, can be applied.

The existence of the bijection between the indistinguishable-particle picture and the distinguishable-particle picture for both bipartite fermions and bipartite bosons was proved in Refs. [31,32]. We apply this bijection to the system of $H_2^+ + e^-$ because the photoelectron is spatially separated from the other electron contained in H_2^+. A generalized bijection between two pictures for multipartite systems including the effect of measurement setups was given in Ref. [33].

Because of the spatial separation of two electrons, we can introduce a localized wave packet, $|\phi_k\rangle$, representing an ejected photoelectron whose distance from the rest of the system, H_2^+, is sufficiently large so that they fulfill the orthogonality, $\langle\eta_l|\phi_k\rangle = 0$. Then, we define two projection operators,

$$\mathcal{P}_1 \equiv \sum_l |\eta_l\rangle_{11}\langle\eta_l|, \qquad \mathcal{Q}_2 \equiv \sum_k |\phi_k\rangle_{22}\langle\phi_k|, \tag{2}$$

and by using a map defined as

$$\sqrt{2}\mathcal{P}_1 \otimes \mathcal{Q}_2, \tag{3}$$

we can map $|\Psi\rangle$ onto the distinguishable-particle picture [32] as

$$\begin{aligned}|\Phi\rangle &\equiv \sqrt{2}\mathcal{P}_1 \otimes \mathcal{Q}_2|\Psi\rangle \\ &= \sum_{hlk} c_{hlk}|\zeta_h\rangle \otimes \frac{1}{\sqrt{2}}\{|\eta_l,\alpha\rangle_1 \otimes |\phi_k,\beta\rangle_2 \\ &\quad - |\eta_l,\beta\rangle_1 \otimes |\phi_k,\alpha\rangle_2\}.\end{aligned} \tag{4}$$

Then, we perform the basis transformation from the set of $\{|\zeta_h\rangle, |\eta_l\rangle\}$ to the vibrational eigenstate of H_2^+, $\{|\chi_v\rangle\}$, as

$$|\Phi\rangle = \sum_{vk} a_{vk}\frac{1}{\sqrt{2}}\{|\chi_v,\alpha\rangle_1 \otimes |\phi_k,\beta\rangle_2 - |\chi_v,\beta\rangle_1 \otimes |\phi_k,\alpha\rangle_2\}, \tag{5}$$

where v is the vibrational quantum number. We note that $|\chi_v\rangle$ includes the spatial part of the remaining electron. Now we can treat $|\Phi\rangle$ as a bipartite system composed of two distinguishable particles, a photoelectron and H_2^+.

Because we use the dipole approximation for the light-matter interaction, the spin state does not change during and after the light-matter interaction, and consequently, the spin entanglement is invariant. Therefore, in order to evaluate the laser parameter dependence of the entanglement, we only need the density matrix for the spatial part, which we can obtain by taking the trace over the spin coordinates, σ_1 and σ_2, as

$$\rho \equiv \mathrm{Tr}_{\sigma_1,\sigma_2}[|\Phi\rangle\langle\Phi|] = \sum_{vv'kk'} a_{vk}a^*_{v'k'}\{|\chi_v\rangle\langle\chi_{v'}| \otimes |\phi_k\rangle\langle\phi_{k'}|\}. \tag{6}$$

Without loss of generality, we can neglect the spin part and concentrate on the spatial part of the state,

$$|\Phi_S\rangle = \sum_{vk} a_{vk}|\chi_v\rangle \otimes |\phi_k\rangle, \tag{7}$$

because $|\Phi_S\rangle\langle\Phi_S|$ gives the same density matrix as Eq. (6). Therefore, we will use the spatial part $|\Phi_S\rangle$, instead of $|\Phi\rangle$ given by Eq. (5), in the following discussion.

The entanglement of the bipartite system can be evaluated by the reduced density matrix of either one of two subsystems. The reduced density matrix of the vibrational state of $H_2{}^+$ is obtained by taking the trace over the photoelectron coordinate as

$$\rho_{\rm vib} = {\rm Tr}_e(\rho) = \sum_{v,v'=0}^{v_{\rm max}} \sum_{k=1}^{k_{\rm max}} a_{vk} a_{v'k}^* |\chi_v\rangle\langle\chi_{v'}|, \tag{8}$$

and that for the spatial part of the photoelectron is obtained as

$$\rho_e = {\rm Tr}_{\rm vib}(\rho) = \sum_{k,k'=1}^{k_{\rm max}} \sum_{v=0}^{v_{\rm max}} a_{vk} a_{vk'}^* |\phi_k\rangle\langle\phi_{k'}|. \tag{9}$$

As a quantitative measure of the extent of entanglement [5,34,35], quantifiers such as purity [36], Von Neumann entropy [37], and measurement-induced disturbance [38] have been proposed. Among these quantifiers, we choose purity of the reduced density matrix because it is directly related to the coherence of the subsystem as shown below. The purity P of $\rho_{\rm vib}$ is defined as the trace of $\rho_{\rm vib}^2$,

$$P \equiv {\rm Tr}\left(\rho_{\rm vib}^2\right) = \sum_{v,v'=0}^{v_{\rm max}} \left| \sum_{k=1}^{k_{\rm max}} a_{vk} a_{v'k}^* \right|^2. \tag{10}$$

When $H_2{}^+$ and e^- are nonentangled, $P = 1$ while it decreases as the extent of entanglement between $H_2{}^+$ and e^- increases, and the minimum of the purity $P_{\rm min}$ is equal to $P_{\rm min} = 1/N$, where $N = \min[v_{\rm max} + 1,\ k_{\rm max}]$. We take N as $N = v_{\rm max} + 1$ because the number of the vibrational states is much smaller than the number of the basis functions needed for expanding the spatial part of the photoelectron. The purity can also be calculated by the reduced density matrix of the spatial part of the photoelectron in the same manner as in Eq. (10) as

$$P = {\rm Tr}\left(\rho_e^2\right). \tag{11}$$

Off-diagonal elements of the reduced density matrix are called the coherence while the diagonal elements are called the population. Equation (10) can be decomposed into two, that is, the first term defined as the sum of the squared modulus of the populations and the second term defined as the sum of the squared modulus of the coherences, as

$$P = \sum_{v=0}^{v_{\rm max}} |(\rho_{\rm vib})_{vv}|^2 + \sum_{v\neq v'}^{v_{\rm max}} |(\rho_{\rm vib})_{vv'}|^2 \equiv P_1 + P_2. \tag{12}$$

In order to evaluate the correlation between two vibrational states, we introduce the degree of coherence [22,24] defined as

$$(\tilde{\rho}_{\rm vib})_{vv'} \equiv \frac{|(\rho_{\rm vib})_{vv'}|}{\sqrt{(\rho_{\rm vib})_{vv}(\rho_{\rm vib})_{v'v'}}} \quad \text{or} \quad 0, \tag{13}$$

which satisfies $0 \leqslant (\tilde{\rho}_{\rm vib})_{vv'} \leqslant 1$. In Eq. (13), we define $(\tilde{\rho}_{\rm vib})_{vv'} = 0$ when $(\rho_{\rm vib})_{vv} = 0$ or $(\rho_{\rm vib})_{v'v'} = 0$ because $a_{vk} = 0,\ \forall k$ should hold if $(\rho_{\rm vib})_{vv} = \sum_{k=1}^{k_{\rm max}} |a_{vk}|^2 = 0$ is satisfied, and consequently, $(\rho_{\rm vib})_{vv'} = \sum_{k=1}^{k_{\rm max}} a_{vk} a_{v'k}^* = 0$ is also satisfied.

From Eqs. (12) and (13), the purity can be related to the degree of coherence as

$$P = \sum_{v=0}^{v_{\rm max}} |(\rho_{\rm vib})_{vv}|^2 + \sum_{v\neq v'}^{v_{\rm max}} (\tilde{\rho}_{\rm vib})_{vv'}{}^2 (\rho_{\rm vib})_{vv} (\rho_{\rm vib})_{v'v'}. \tag{14}$$

When the population is equally distributed, i.e., $(\rho_{\rm vib})_{vv} = 1/v_{\rm max}$ for all v, the purity takes the minimum value of $P_{\rm min} = 1/v_{\rm max}$ and the degree of coherence is zero. If the degree of coherence takes its maximum value, i.e., $(\tilde{\rho}_{\rm vib})_{vv'} = 1$ for all v and v', the purity becomes unity as

$$\begin{aligned} P &= \sum_{v=0}^{v_{\rm max}} |(\rho_{\rm vib})_{vv}|^2 + \sum_{v\neq v'}^{v_{\rm max}} (\rho_{\rm vib})_{vv} (\rho_{\rm vib})_{v'v'} \\ &= \left| \sum_{v=0}^{v_{\rm max}} (\rho_{\rm vib})_{vv} \right|^2 = 1, \end{aligned} \tag{15}$$

meaning that the total system is nonentangled.

B. Numerical procedure

After separating out the motion of the center of mass, the Hamiltonian of H_2 interacting with a light field within the dipole approximation is expressed as

$$H = T_0 + V = T_e + T_{\rm N} + V_{eN} + V_{ee} + V_{NN} + V_{\rm int}, \tag{16}$$

where $V_{\rm int}$ is

$$V_{\rm int} = \mu E(t), \tag{17}$$

T_e is the kinetic energy operator of two electrons, T_N is the kinetic energy operator of two nuclei, V_{eN} is the Coulomb attraction between two electrons and two protons, V_{NN} is the Coulomb repulsion between two protons, μ is the electric dipole, and $E(t)$ is the linearly polarized electric field of light whose polarization direction is along the one-dimensional axis.

The explicit form of the operators is expressed as

$$T_e + T_N = -\frac{1}{2\mu_e}\left(\frac{\partial^2}{\partial x^2} + \frac{\partial^2}{\partial y^2}\right) - \frac{1}{M}\frac{\partial^2}{\partial R^2}, \tag{18a}$$

$$\begin{aligned} V_{eN} = &-\frac{1}{\sqrt{\left(x - \frac{R}{2}\right)^2 + \alpha(R)}} - \frac{1}{\sqrt{\left(x + \frac{R}{2}\right)^2 + \alpha(R)}} \\ &- \frac{1}{\sqrt{\left(y - \frac{R}{2}\right)^2 + \alpha(R)}} - \frac{1}{\sqrt{\left(y + \frac{R}{2}\right)^2 + \alpha(R)}}, \end{aligned} \tag{18b}$$

$$V_{ee} = \frac{1}{\sqrt{(x-y)^2 + \beta}}, \tag{18c}$$

$$V_{NN} = \frac{1}{R}, \tag{18d}$$

where x and y are the coordinates of the two electrons whose origin is located at the center of mass of the nuclei, R is the internuclear distance, $M = 1.836 \times 10^3$ a.u. is the mass of

TABLE I. The ten sets of the laser parameters.

Number of set	Wavelength (nm)	Number of cycles[a]	T_{pulse} (fs)	Intensity[b] (W cm^{-2})	Keldysh parameter γ[c]
1	90	20	6.0	5×10^{12}	39
2				10^{13}	28
3				10^{15}	2.8
4		3	0.9	10^{13}	28
5	40	20	2.7	10^{13}	63
6				10^{15}	6.3
7		3	0.4	10^{15}	
8	20	40	2.7	10^{15}	12
9		20	1.3	10^{15}	
10				10^{16}	3.9

[a]At the central wavelength of 20 nm, the three-cycle pulse is not considered because its bandwidth becomes so large that it can generate a very fast electron and a quarter of the de Broglie wavelength ($\frac{\lambda_{\text{dB}}}{4} \cong 0.8 - 0.9$ a.u.) is comparable with the grid spacing of the electronic coordinate (0.5 a.u.).

[b]The peak intensities are set so that loss of the population in the ground state of H_2 defined as $1 - \langle \Phi_0^{H_2} | \Phi(T) \rangle$ is in the range between 10^{-4} and 10^{-1} except set 3.

[c]The Keldysh parameter is defined as $\gamma \equiv \sqrt{I_P/2U_P}$, where I_P is the ionization potential of the H_2 ground state and U_P is the ponderomotive energy.

a proton, and $\mu_e = 2M/(2M+1)$ is the reduced mass of an electron. The dipole operator μ is defined as $\mu = x + y$. The soft-core potential [39] is applied for V_{eN} and V_{ee}, in which the Coulomb singularities are eliminated by the softening parameters, $\alpha(R)$ and β. The parameter $\alpha(R)$ is determined so that the $1s\sigma_g$ potential energy curve of H_2^+ [40] is reproduced. On the other hand, β is determined so that the equilibrium internuclear distance of H_2 in the electronic ground state, $R_{\text{eq}}^{\text{ref.}} = 1.401$ a.u. [40], is reproduced. We solve the TDSE numerically with a grid method called the symmetry-adapted grid method that we have developed to efficiently calculate single-ionization processes in atoms and molecules (see Appendix A).

In the present model, Φ_S is a function of (x, y, R), ϕ_k is a function of x, and χ_v is a function of (y, R). Because we can adopt any type of complete orthonormal basis to describe a photoelectron in the calculation of ρ_{vib} as long as the basis has a vanishing overlap with the basis set describing the other electron bound to the H_2^+ core, we adopt the grid basis as a complete orthonormal basis with which we describe the subsystem of a photoelectron, and rewrite Eq. (7) as

$$|\Phi_S\rangle = \sum_{v=0}^{v_{\max}} \sum_{k=1}^{d_e} \tilde{a}_{vk} |\chi_v\rangle \otimes |x_k\rangle, \tag{19}$$

where d_e is the number of grid points along the x axis. The grid basis $\{|x_k\rangle\}$ satisfies

$$\langle y, R | \langle x_k | \Phi_S \rangle = \Phi_S(x_k, y, R) \Delta_x^{1/2}, \tag{20}$$

where Δ_x is the grid spacing along the x axis. The reduced density matrix is expressed as

$$\rho_{\text{vib}} = \text{Tr}_e(|\Phi_S\rangle\langle\Phi_S|) = \sum_{v,v'=0}^{v_{\max}} \sum_{k=1}^{d_e} \tilde{a}_{vk} \tilde{a}_{v'k}^* |\chi_v\rangle\langle\chi_{v'}|. \tag{21}$$

The details of the numerical procedure to calculate the reduced density matrix are given in Appendixes A and B.

III. RESULTS AND DISCUSSION

A. Entanglement and coherence: Pulse duration dependence and wavelength dependence

The purity and the degree of coherence are calculated using the ten different sets of laser parameters listed in Table I. The laser parameters are chosen so that the Keldysh parameter satisfies $\gamma > 2$, which means that the contribution from the tunnel ionization can be neglected. The definition of T_{pulse} is given by Eq. (B3) in Appendix B. As shown in Fig. 1, the purity increases as the pulse duration decreases, or equivalently, as the spectral bandwidth increases, reflecting the fact that it becomes difficult to specify which one of the vibrational states is prepared only by projecting the photoelectron on its energy eigenstate.

In Fig. 2, we show the degree of coherence between the vibrational ground state and the vth vibrational state, $(\tilde{\rho}_{\text{vib}})_{v,0}$, as a function of the vibrational quantum number v. It can be seen that the degree of coherence decreases as the vibrational quantum number increases. It can also be seen in Fig. 2 that the degree of coherence decreases as the pulse duration increases for the same v.

When the bandwidth of the laser pulse is smaller than the energy gap between the ground and the vth state, it becomes less probable for the pair of vibrational states to be populated coherently. Therefore, the degree of coherence decreases when the bandwidth decreases by increasing the pulse duration or when the energy gap between the vth level and the ground vibrational state increases by increasing the vibrational quantum number. When the bandwidth becomes extremely small so that the respective vibrational states are exclusively assigned to the specific kinetic energies of the photoelectron, that is, when $a_{vk} a_{v'k}^* \propto \delta_{vv'}$ is satisfied, $(\rho_{\text{vib}})_{vv'} \propto \delta_{vv'}$ holds from Eq. (8), representing that the degree of coherence is zero.

In Fig. 1, in the case of $\lambda = 40$ nm and $N = 20$ cycles (set 6: open circle) and in the case of $\lambda = 20$ nm and $N = 40$

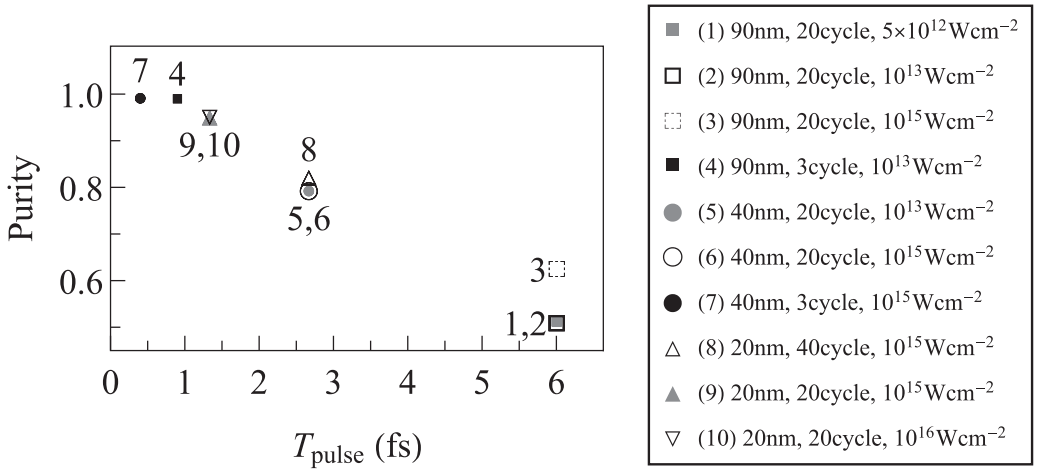

FIG. 1. The purity as a function of the pulse duration for the ten different sets of laser parameters. In the linear regime, the purity is insensitive to the light-field intensity; e.g., in the case of ($\lambda = 20$ nm, $N = 20$ cycles), the purity at 10^{15} W cm^{-2} (set 9: filled triangle) and the purity at 10^{16} W cm^{-2} (set 10: open triangle) take the same values of 0.954. Similarly, in the case of ($\lambda = 40$ nm, $N = 20$ cycles), the purity at 10^{13} W cm^{-2} (set 5: filled circle, $P = 0.796$) and the purity at 10^{15} W cm^{-2} (set 6: open circle, $P = 0.795$) are very close to each other.

cycles (set 8: open triangle), the purities are 0.795 and 0.825, respectively. As shown in Fig. 2, because the degrees of coherence of these two cases are almost the same, reflecting the fact that their pulse durations are the same, the small difference in their purities can be ascribed to the difference in the populations. The dependence of the degree of coherence on the pulse duration is consistent with the previous study on the ionization of Xe [24], in which the degree of coherence between two levels of Xe^+ was shown to decrease as the pulse duration increases.

B. Entanglement and coherence: Intensity dependence

1. Linear regime

We investigate the light-field intensity dependence of the purity and the degree of coherence in the cases of set 1 and set 2 with $\lambda = 90$ nm and $N = 20$ cycles. As shown in Fig. 2, the degree of coherence at the light-field intensity of 10^{13} W cm^{-2} (set 2: open square) exhibits almost the same dependence on the vibrational quantum number as the degree of coherence at the light-field intensity of 5×10^{12} W cm^{-2} (set 1: filled square), reflecting the fact that their pulse durations are the same. Because their purities are almost the same as shown in Fig. 1, the populations in sets 1 and 2 are expected to be almost the same, which means that the light-field intensities are in the linear regime; that is, the loss of the population in the ground state of H_2 as well as the populations in the vibrationally excited states of H_2^+ increase linearly in this intensity range by a process corresponding to a one-photon absorption. Indeed, we have confirmed that the loss of the population in the ground state of H_2 defined as $1 - \langle \Phi_0^{H_2} | \Phi(T) \rangle$ is 0.033 and 0.016 at 10^{13} W cm^{-2} and 5×10^{12} W cm^{-2}, respectively.

We can also see in Figs. 1 and 2 that, when the light-field intensity is in the linear regime, the purity and the degree of coherence obtained using two different sets of the wavelength

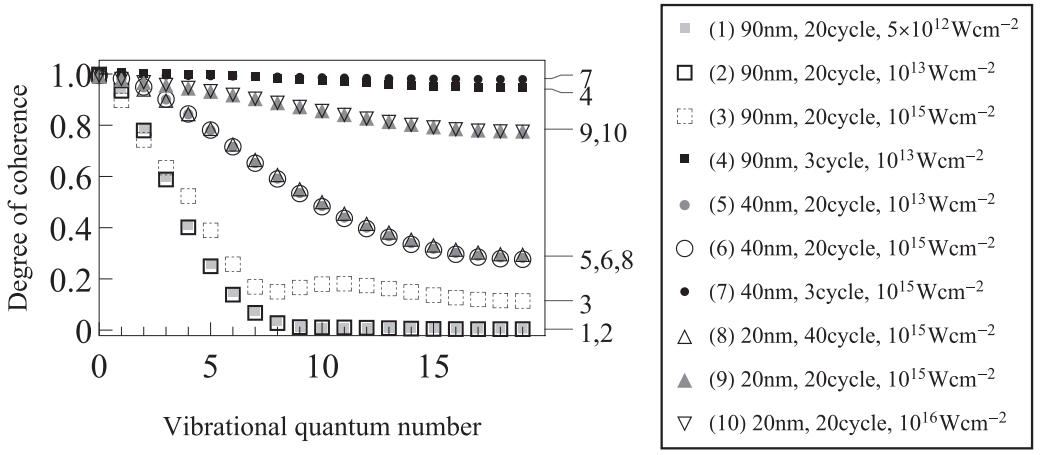

FIG. 2. The degree of coherence $(\tilde{\rho}_{\text{vib}})_{v,0}$ as a function of vibrational quantum number and the pulse duration for ten different laser parameters. In the linear regime, the degree of coherence is insensitive to the light-field intensity, e.g., in the case of ($\lambda = 20$ nm, $N = 20$ cycles), the degree of coherence at 10^{15} W cm^{-2} (set 9: filled triangle) is in good agreement with the degree of coherence at 10^{16} W cm^{-2} (set 10: open triangle). Similarly, in the case of ($\lambda = 40$ nm, $N = 20$ cycles), the degree of coherence at 10^{13} W cm^{-2} (set 5: filled circle) is in good agreement with the degree of coherence at 10^{15} W cm^{-2} (set 6: open circle).

and the number of cycles, i.e., (i) set 9 and set 10 ($\lambda = 20$ nm, $N = 20$ cycles) and (ii) set 5 and set 6 ($\lambda = 40$ nm, $N = 20$ cycles), do not vary sensitively on the light-field intensity.

2. Nonlinear regime

As shown in Fig. 2, in the case of $\lambda = 90$ nm and $N = 20$ cycles, the degree of coherence at $10^{15}\,\mathrm{W\,cm^{-2}}$ (set 3: open dashed square) deviates largely from the other two cases at $5 \times 10^{12}\,\mathrm{W\,cm^{-2}}$ (set 1) and $10^{13}\,\mathrm{W\,cm^{-2}}$ (set 2). At $10^{15}\,\mathrm{W\,cm^{-2}}$, the $(\tilde{\rho}_{\mathrm{vib}})_{v,0}$ values for $v = 1$ and 2 are almost the same as the corresponding values for the weaker two cases, but, as the vibrational quantum number increases further, for $v \geqslant 3$, the $(\tilde{\rho}_{\mathrm{vib}})_{v,0}$ value at $10^{15}\,\mathrm{W\,cm^{-2}}$ becomes larger than the corresponding values at $5 \times 10^{12}\,\mathrm{W\,cm^{-2}}$ and $10^{13}\,\mathrm{W\,cm^{-2}}$, and the deviation becomes maximum when the vibrational quantum number is $v \sim 11$. This deviation can be ascribed to the second- or higher-order interaction with the light field as described below.

The loss of the ground state of H_2 at $10^{15}\,\mathrm{W\,cm^{-2}}$ (set 3) is 0.94, which is much larger than the loss of the ground state at $5 \times 10^{12}\,\mathrm{W\,cm^{-2}}$ (set 1) and that at $10^{13}\,\mathrm{W\,cm^{-2}}$ (set 2), showing that the light-field intensity of $10^{15}\,\mathrm{W\,cm^{-2}}$ is no longer in the linear regime. The Keldysh parameter, $\gamma = 2.8$ (see Table I), for set 3 indicates that the photoionization proceeds through the multiphoton process.

Because the transition moment between the ground state of H_2 and the final state composed of the photoelectron and the vibrational state of $H_2{}^+(1s\sigma_g)$ decreases as the photoelectron energy increases, the ionization probability at 90 nm is larger than the ionization probabilities at the other shorter wavelengths as long as the number of cycles and the intensity are the same. Therefore, at a 90-nm laser pulse, the second- or higher-order interaction can no longer be neglected at the intensity reaching $10^{15}\,\mathrm{W\,cm^{-2}}$.

At $10^{15}\,\mathrm{W\,cm^{-2}}$, the second-order interaction with the light field, corresponding to the two-photon process, results in a broader energy distribution of photoelectrons than that of photoelectrons produced from a one-photon process. Therefore, it is expected that the second-order interaction increases the coherence among the vibrational states of $H_2{}^+$. On the other hand, the third-order interaction with the light field, corresponding to a three-photon process, increases the coherence not only by creating the photoelectron with a broader energy distribution but also by inducing one-photon ionization followed by Raman-type vibrational excitations.

For instance, if the ionization results in the formation of $|\chi_v\rangle|\phi_k\rangle$, a Raman-type transition from $|\chi_v\rangle|\phi_k\rangle$ to $|\chi_{v'}\rangle|\phi_k\rangle$ can occur. Consequently, it becomes more probable that the vth and the v'th states are assigned to the same kinetic energy of the photoelectron; therefore, $a_{vk}a^*_{v'k} \neq 0$ holds in the wider range of k than in the case of the weaker intensities, resulting in the higher coherence.

C. Purity, coherence, and population

As shown in Fig. 1, when $\lambda = 90$ nm and $N = 20$ cycles, the purity at $10^{15}\,\mathrm{W\,cm^{-2}}$ (set 3, $P = 0.626$) is larger by $0.115 - 0.116$ than the purities at $5 \times 10^{12}\,\mathrm{W\,cm^{-2}}$ (set 1, $P = 0.511$) and $10^{13}\,\mathrm{W\,cm^{-2}}$ (set 2, $P = 0.510$). At $10^{15}\,\mathrm{W\,cm^{-2}}$, because of the transitions among the vibrational states induced by the light field, not only the coherence but also the population can be different from the weaker cases. In order to evaluate the contribution from the population and that from the coherence to the purity, we use the sum of the squared modulus of the population P_1 and the sum of the squared modulus of the coherence P_2 defined in Eq. (12).

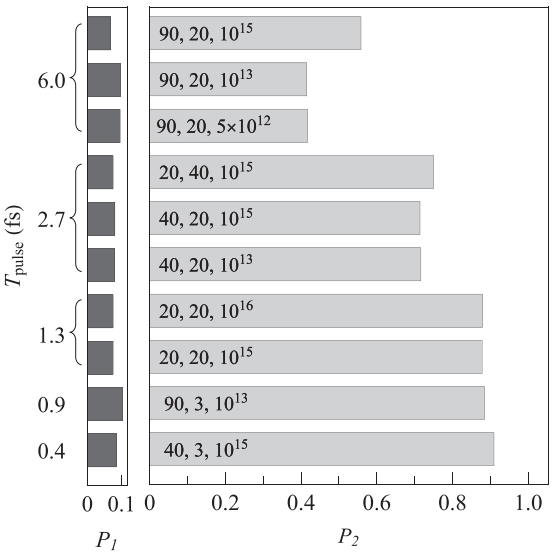

FIG. 3. The two contributions to the purity, the population P_1 and the coherence P_2, for the ten different laser parameters. The number inside the bar indicates the laser parameters, e.g., the set of "40, 3, and 10^{15}" represents the pulse characterized by the parameters of 40 nm, 3 cycles, and $10^{15}\,\mathrm{W\,cm^{-2}}$.

As shown in Fig. 3, the P_2 value at $10^{15}\,\mathrm{W\,cm^{-2}}$ (set 3) is larger than the P_2 values at $5 \times 10^{12}\,\mathrm{W\,cm^{-2}}$ (set 1) and $10^{13}\,\mathrm{W\,cm^{-2}}$ (set 2), which is consistent with the above explanation about the increase in the degree of coherence. On the other hand, the contribution from the P_1 value at $10^{15}\,\mathrm{W\,cm^{-2}}$ is smaller than the P_1 values at $5 \times 10^{12}\,\mathrm{W\,cm^{-2}}$ and $10^{13}\,\mathrm{W\,cm^{-2}}$. The smaller value of P_1 means that the population is more equally distributed associated with the Raman-type transitions among the vibrational states. Because the amount of decrease in P_1 is much smaller than the amount of increase in P_2, the purity defined as the sum of P_1 and P_2 becomes larger at $10^{15}\,\mathrm{W\,cm^{-2}}$ than those at $5 \times 10^{12}\,\mathrm{W\,cm^{-2}}$ and $10^{13}\,\mathrm{W\,cm^{-2}}$.

As shown in Fig. 3, the contribution from P_2 is much larger than that from P_1 in all the ten cases of the laser parameters. Because the pulse durations considered here are all short enough, the bandwidths of the laser are wider than the energy gaps among the vibrational states of $H_2{}^+$, which results in the large coherence. When the pulse duration becomes longer so that the bandwidth becomes comparable with or smaller than the energy gaps among the vibrational states, the contribution from P_1 to the purity becomes larger. In an extreme case of the infinitely long pulse duration, corresponding to a continuous wave (cw) laser, the coherence P_2 between vibrational states vanishes, and consequently, the purity is represented by the population P_1 exclusively.

D. Experimental scheme for determining the reduced density matrix

The reduced density matrix of the vibrational states can be determined by the pump-probe experiment as proposed in Ref. [41]. First, H_2 is ionized by the pump pulse and the resultant vibrational state of $H_2{}^+$ is described using $\rho_{\rm vib}$ as in Eq. (8). After a certain time delay τ, the probe VUV pulse excites $H_2{}^+$ to the $2p\sigma_u$ state and the photofragment, H^+, is produced via the dissociation. We set the origin of time, $t = 0$, at the peak position of the temporal shape of the pump pulse and set the peak position of the probe pulse at $t = \tau$.

By assuming that the electric field of the probe pulse, $E_{\rm probe}$, satisfies $E_{\rm probe}(t-\tau) \neq 0$ during $t \in [t_0, t_f]$, the free propagation until the system is excited by the probe pulse is expressed by

$$U_{\rm free}(\tau) = \exp\left[-iH_0\left(\tau - \frac{T_{\rm pulse} + t_f - t_0}{2}\right)\right], \tag{22}$$

where H_0 is the field-free Hamiltonian for $H_2{}^+$ and $T_{\rm pulse}$ is the duration of the pump pulse defined in Eq. (B3) in Appendix B. The interaction with the probe pulse is expressed in the first-order perturbation theory as

$$U_{\rm probe}(t) = \left[e^{-iH_0(t-t_0)} - i\int_{t_0}^{t} dt_1 e^{-iH_0(t-t_1)} V_{\rm int}(t_1) e^{-iH_0(t_1-t_0)}\right], \tag{23}$$

with

$$V_{\rm int}(t_1) = \mu E_{\rm probe}(t_1 - \tau), \tag{24}$$

where the probe pulse $E_{\rm probe}(t_1 - \tau)$ starts interacting with $H_2{}^+$ at $t_1 = t_0$ and ends interacting at $t_1 = t_f$.

The observation of $|\chi^u(\omega^u)\rangle$, which is the dissociating eigenstate of $2p\sigma_u$ having the kinetic energy release (KER), ω^u, is expressed using the projection operator $\Pi_{\rm u} \equiv |\chi^u(\omega^u)\rangle\langle\chi^u(\omega^u)|$ as

$$\begin{aligned}
&\Pi_u U_{\rm probe} U_{\rm free}(\tau) \rho_{\rm vib} U_{\rm free}^\dagger(\tau) U_{\rm probe}^\dagger \Pi_u \\
&= |\chi^u\rangle \sum_{v,v'=0}^{v_{\rm max}} (\rho_{\rm vib})_{vv'} e^{-i(\omega_v - \omega_{v'})(\tau - \frac{T_{\rm pulse}+t_f-t_0}{2})} \\
&\quad \times \langle\chi^u|U_{\rm probe}|\chi_v\rangle\langle\chi_{v'}|U_{\rm probe}^\dagger|\chi^u\rangle\langle\chi^u| \\
&= |\chi^u\rangle \sum_{v,v'=0}^{v_{\rm max}} (\rho_{\rm vib})_{vv'} e^{-i(\omega_v - \omega_{v'})(\tau - \frac{T_{\rm pulse}+t_f-t_0}{2})} \\
&\quad \times p_v(\omega^u) p_{v'}^*(\omega^u) \langle\chi^u|,
\end{aligned} \tag{25}$$

where ω_v is the eigenenergy of the vth vibrational state and $p_v(\omega^u)$ is the transition amplitude from $|\chi_v\rangle$ to $|\chi^u\rangle$ defined as

$$p_v(\omega^u) = -iM_v(\omega^u) e^{-i\omega^u t} e^{i\omega_v t_0} \int_{t_0}^{t} dt_1 E_{\rm probe}(t_1 - \tau) e^{i(\omega^u - \omega_v)t_1}, \tag{26}$$

using the transition moment,

$$M_v(\omega^u) \equiv \langle\chi^u|\mu|\chi_v\rangle. \tag{27}$$

The probability of finding $|\chi^u\rangle$ by the detector is a function of the time delay τ and the KER, ω^u, expressed as

$$I(\tau;\omega^u) \equiv \sum_{v,v'=0}^{v_{\rm max}} (\rho_{\rm vib})_{vv'} e^{-i\omega_{vv'}(\tau - \frac{T_{\rm pulse}+t_f-t_0}{2})} p_v(\omega^u) p_{v'}^*(\omega^u), \tag{28}$$

where we defined $\omega_{vv'} \equiv \omega_v - \omega_{v'}$. This probability corresponds to the delay-KER spectrogram defined in Ref. [41]. Because the pulse duration of the probe pulse is short enough so that $E_{\rm probe}(t_1 - \tau) = 0$ is satisfied when $t_1 < t_0$ or $t_1 > t_f$, the time integral in Eq. (26) becomes the Fourier transform of the probe pulse represented as

$$\begin{aligned}
p_v(\omega^u) &= -iM_v(\omega^u) e^{-i\omega^u t} e^{i\omega_v t_0} e^{i(\omega^u - \omega_v)\tau} \\
&\quad \times \int_{t_0-\tau}^{t-\tau} dt' E_{\rm probe}(t') e^{i(\omega^u - \omega_v)t'} \\
&= -iM_v(\omega^u) e^{-i\omega^u(t-\tau)} e^{-i\omega_v(\tau - t_0)} \\
&\quad \times \int_{-\infty}^{\infty} dt' E_{\rm probe}(t') e^{i(\omega^u - \omega_v)t'} \\
&= -iM_v(\omega^u) e^{-i\omega^u(t-\tau)} e^{-i\omega_v \frac{t_f - t_0}{2}} \tilde{E}(\omega^u - \omega_v),
\end{aligned} \tag{29}$$

where $\tilde{E}(\omega)$ is the Fourier amplitude of the probe pulse.

By representing $p_v(\omega^u)$ and $p_{v'}^*(\omega^u)$ in Eq. (28) by Eq. (29) and by performing the Fourier transform with respect to τ, we obtain the frequency-KER spectrogram as

$$\begin{aligned}
\tilde{I}(\Omega;\omega^u) &= \sum_{v=0}^{v_{\rm max}} (\rho_{\rm vib})_{vv} |M_v(\omega^u)\tilde{E}(\omega^u - \omega_v)|^2 \delta(\Omega) \\
&\quad + \sum_{v,v'=0}^{v_{\rm max}} \{\tilde{I}_{vv'}(\Omega;\omega^u) + \tilde{I}_{vv'}(-\Omega;\omega^u)\},
\end{aligned} \tag{30}$$

where $\tilde{I}_{vv'}(\Omega;\omega^u)$ is defined as

$$\begin{aligned}
\tilde{I}_{vv'}(\Omega;\omega^u) &= (\rho_{\rm vib})_{vv'} e^{i\omega_{vv'}\frac{T_{\rm pulse}}{2}} M_v(\omega^u) M_{v'}^*(\omega^u) \\
&\quad \times \tilde{E}(\omega^u - \omega_v)\tilde{E}^*(\omega^u - \omega_{v'})\delta(\Omega - \omega_v + \omega_{v'}).
\end{aligned} \tag{31}$$

The left-hand side of Eq. (31) above, $\tilde{I}_{vv'}(\Omega;\omega^u)$, gives the nonzero complex amplitude only when $\Omega = \omega_{vv'}$, $\omega^u \cong \omega_p + \omega_v$, and $\omega^u \cong \omega_p + \omega_{v'}$ are satisfied, where ω_p represents the frequency component of the probe pulse. Because $\tilde{E}(\omega^u - \omega_v)$ and $\tilde{E}^*(\omega^u - \omega_{v'})$ in Eq. (31), varying as a function of ω^u, have the same width, the peak in $\tilde{I}_{vv'}(\Omega;\omega^u)$ at the beat frequency of $\omega_{vv'}$ is spread along the ω^u axis with the width of the product of $\tilde{E}(\omega^u - \omega_v)\tilde{E}^*(\omega^u - \omega_{v'})$. Therefore, in order to obtain the reduced density matrix element, $(\rho_{\rm vib})_{vv'}$, from the frequency-KER spectrogram, the bandwidth of the probe pulse should be larger than $\omega_{vv'}$. In other words, the pulse duration of the probe pulse should be shorter than the beat period defined as $2\pi/\omega_{vv'}$ in the time domain. This means that, in order to obtain the entire reduced density matrix of $\rho_{\rm vib}$, the pulse duration of the probe laser pulse needs to be shorter than the shortest beat period of $2\pi/\omega_{0,v_{\rm max}} = 1.5$ fs.

In the frequency-KER spectrogram, there are peaks at the zero frequency $\Omega = 0$ and at the beat frequencies $\Omega = \omega_{vv'}$

as can be seen from Eq. (30). As long as the Fourier amplitude of the probe pulse $\tilde{E}(\omega)$ is known, the diagonal elements, $(\rho_{\rm vib})_{vv}$, and the off-diagonal elements, $(\rho_{\rm vib})_{vv'}$, of the reduced density matrix are determined using the transition amplitude $M_v(\omega^u)$, which can be evaluated numerically from the first and second terms in Eq. (30), respectively. The purity and the degree of coherence can be calculated from Eqs. (10) and (13), respectively, using the reduced density matrix. We note that, even if the Fourier transform of the probe pulse is not known in advance, the matrix elements of the reduced density matrix can be determined from the frequency-KER spectrogram using the iterative method recently proposed in Refs. [41,42].

As described above, we can extract the purity and the degree of coherence experimentally in the following steps. First, we ionize H_2 by the irradiation of an ultrashort XUV pulse, dissociate the resultant H_2^+ by the irradiation of a subsequent probe VUV pulse, and record the KER distribution of the photofragment, H^+. Then, by performing the Fourier transform of the delay-KER spectrum, we obtain a frequency-KER spectrogram and extract the matrix elements of the reduced density matrix of $\rho_{\rm vib}$ from Eq. (30). Finally, we calculate the purity and the degree of coherence from Eqs. (10) and (13), respectively, using the reduced density matrix.

IV. CONCLUSION

We have investigated theoretically the photoionization process of H_2 induced by the irradiation of an ultrashort XUV laser pulse by regarding H_2^+ and a photoelectron as a bipartite system, and have analyzed the relation between the purity, which quantifies the entanglement between H_2^+ and the photoelectron, and the coherence in the vibrational states of the moiety of H_2^+.

We perform one-dimensional propagation of the wave packet represented by the grid basis to describe the ionization of H_2 and demonstrate how the purity and the coherence depend on the laser parameters in the range of I (peak field intensity)$= 5 \times 10^{12} - 10^{16}\,\mathrm{W\,cm^{-2}}$, λ (the central wavelength) $= 20 - 90$ nm, and $T_{\rm pulse}$ (the pulse duration) $= 0.4 - 6.0$ fs.

(i) As the pulse duration increases the degree of coherence decreases, reflecting the fact that it becomes less probable for the two states to be coherently populated. The degree of coherence also decreases as the energy gap between the two vibrational states increases by the same reason.

(ii) As long as the laser intensity is weak enough so that the loss of the population in the ground state of H_2 depends linearly on the laser intensity, the purity and the coherence are insensitive to the peak intensity of the laser pulse. On the other hand, when the laser intensity becomes so strong that the Raman-type transitions among the vibrational states of H_2^+ cannot be neglected, the purity and the degree of coherence vary depending on the laser intensity. In the case of $\lambda = 90$ nm and $N = 20$ cycles, both the degree of coherence and the purity increase when the laser intensity is raised to $I = 10^{15}\,\mathrm{W\,cm^{-2}}$ from $5 \times 10^{12}\,\mathrm{W\,cm^{-2}}$ and $10^{13}\,\mathrm{W\,cm^{-2}}$.

(iii) When the pulse duration is short enough so that the bandwidth of the pulse is comparable to or larger than the energy gaps between the vibrational states of H_2^+, the coherence makes the dominant contribution to the purity while the population makes the minor contribution. Because the extent of the entanglement increases when the purity decreases, the extent of the entanglement between the vibrational states of H_2^+ and the photoelectron increases as the coherence among the vibrational states decreases as long as the pulse duration is short enough so that the bandwidth is comparable to or larger than the energy gaps between the vibrational states.

(iv) The procedure for deriving the purity and the degree of coherence from experimental data is proposed. Once the experimental delay-KER spectrogram is recorded by pump-probe measurements, the frequency-KER spectrogram is obtained by the Fourier transform, from which the reduced density matrix is obtained. Then, the purity and the degree of coherence are calculated from the matrix elements of the reduced density matrix.

ACKNOWLEDGMENTS

T.N. thanks Dr. Toshihiko Sasaki (Photon Science Center, The University of Tokyo) for his valuable comments on our manuscript. This research was supported by JSPS KAKENHI Grants No. JP18K05024 and No. JP15H05696.

APPENDIX A: SYMMETRY-ADAPTED GRID METHOD

The computational scheme to obtain the reduced density matrix of the vibrational state of H_2^+ is given as follows. First, we propagate the electronic and vibrational ground state of H_2, $|\Phi_0^{H_2}\rangle$, in the light field as

$$|\Phi(t)\rangle = U(t)\big|\Phi_0^{H_2}\big\rangle, \tag{A1}$$

where $U(t)$ is the propagator corresponding to the time-dependent Hamiltonian, Eq. (16), and project out the initial state as

$$|\Phi'(t)\rangle = \big(1 - \big|\Phi_0^{H_2}\big\rangle\big\langle\Phi_0^{H_2}\big|\big)|\Phi(t)\rangle. \tag{A2}$$

We obtain the wave packet corresponding to the single ionization by extracting the part of $|\Phi'(t)\rangle$ in the domain S_1 or S_2 in Fig. 4 at certain time T, which is denoted as $|\Phi_{S1,S2}(T)\rangle$. The domains S_1 and S_2 in which one of the electrons is emitted are defined by $|x| > 30$ a.u. and $|y| < 30$ a.u., while the domain B in which both electrons are bound is defined by $|x| < 30$ a.u. and $|y| < 30$ a.u. In order to analyze $|\Phi_{S1,S2}(t)\rangle$, we wait until T when the singly ionized wave packet can be described well by the product of the eigenstate of H_2^+ and $|x_k\rangle$.

It should be noted that the wave packet $|\Phi_{S1,S2}(T)\rangle$ is composed of (i) a photoelectron and a bound state of $H_2^+(1s\sigma_g)$ and (ii) a photoelectron with the dissociating H_2^+ through the continuum state of H_2^+ $(1s\sigma_g)$ above the dissociation threshold or through the continuum state in an electronically excited state of H_2^+ like $2p\sigma_u$. Considering that the scalar product of $|\chi_v\rangle$ and the dissociating states of H_2^+ included in $|\Phi_{S1,S2}(T)\rangle$ vanish, the projection of $|\Phi_{S1,S2}(T)\rangle$ on $|\chi_v\rangle \otimes |x_k\rangle$ yields $\tilde{a}_{vk}$, that is,

$$\tilde{a}_{vk} = \langle\chi_v|\langle x_k|\Phi_{S1,S2}(T)\rangle. \tag{A3}$$

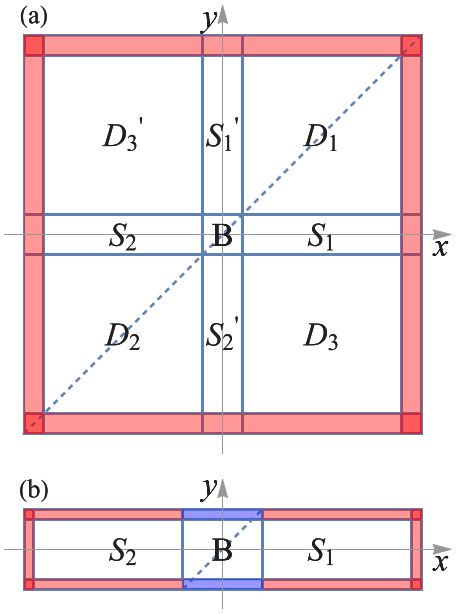

FIG. 4. (a) The grid space in the conventional grid method. In domain B both electrons are bound. The domain S represents single ionization and the domain D represents double ionization. (b) The grid space in the SAG method. The red peripheral region represents the CAP. In the peripheral region (in blue color) above and below the domain B, the reflection is avoided without using the CAP.

By using the property of the grid basis expressed in Eq. (20), we can simplify Eq. (A3) as

$$\begin{aligned}\tilde{a}_{vk} &= \langle\chi_v|\Phi_{\mathrm{S1,S2}}(x_k,T)\rangle\Delta_x^{1/2}\\ &= \sum_{l,m}\langle\chi_v|y_l,R_m\rangle\langle y_l,R_m|\Phi_{\mathrm{S1,S2}}(x_k,T)\rangle\Delta_x^{1/2}\\ &= \sum_{l,m}\chi_v^*(y_l,R_m)\Phi_{\mathrm{S1,S2}}(x_k,y_l,R_m,T)\Delta_y\Delta_R\Delta_x^{1/2}, \quad \text{(A4)}\end{aligned}$$

where $|y_l\rangle$ and $|R_m\rangle$ are the grid bases for the respective coordinates. From Eqs. (21) and (A4), we can obtain the reduced density matrix from which the purity and the degree of coherence are calculated.

We integrate the time-dependent Schrödinger equation numerically by adopting the grid method. We perform the time propagation using the split-operator method expressed as

$$\begin{aligned}U(t) = \exp\left[-i\frac{\Delta t}{2}V\left(t+\frac{\Delta t}{2}\right)\right]\exp(-i\Delta t T_0)\\ \times\exp\left[-i\frac{\Delta t}{2}V\left(t+\frac{\Delta t}{2}\right)\right], \quad \text{(A5)}\end{aligned}$$

where $V(t)$ is the potential including the laser-matter interaction and T_0 is the kinetic energy operator [Eq. (16)]. For the numerical differentiation, we employ the fast Fourier transform (FFT).

Because we neglect the double ionization, the grid space can be reduced significantly. By following the scheme introduced by Rapp and Bauer [43], we developed a symmetry-adapted grid (SAG) method by which we propagate the wave packet described in the two-dimensional grid space [Fig. 4(b)] by making full use of the symmetry property of the electronic wave function. In Fig. 4(a), the domain B represents H_2 in which both electrons are bound, the domain S represents the single ionization, and the domain D represents the double ionization. Because the spatial wave function of the electronic ground singlet state is symmetric under the exchange of the two electron coordinates, the two domains, S_1 and S_1', are equivalent; so are the two domains, S_2 and S_2'. In the SAG method, we can reduce the computational cost significantly. Indeed, the wave packet propagation only in the domains B, S_1, and S_2 [Fig. 4(b)] is sufficient for describing the wave packet corresponding to the single ionization.

In order to avoid the spurious reflection at the edge of the grid space, a complex absorbing potential (CAP) [44] is applied to the red peripheral region in Fig. 4. Because the wave packet being propagated from the domain S into D should be absorbed in the SAG method, the CAP is applied to the red-colored upper and lower boundary regions in Fig. 4(b).

Because the wave packet going into the domain S_1' from B should not be absorbed, the CAP cannot be applied in the blue-colored upper and lower regions in Fig. 4(b). However, if there is no CAP there, a spurious reflection could occur. We can solve this problem by utilizing the symmetry of the wave function and the symmetry of the Hamiltonian under the exchange of two electronic coordinates.

By denoting the wave function after the operation of the first term of the propagator in Eq. (A5) as

$$|\Phi'\rangle \equiv \exp\left\{-i\frac{\Delta t}{2}V\left(t+\frac{\Delta t}{2}\right)\right\}|\Phi\rangle, \quad \text{(A6)}$$

the operation of the second term in the propagator on the wave function reads

$$\begin{aligned}\exp(-i\Delta t T_0)|\Phi'\rangle = \exp\left\{-i\Delta t\frac{1}{M}\frac{\partial^2}{\partial R^2}\right\}\exp\left\{-i\Delta t\frac{1}{2\mu_e}\frac{\partial^2}{\partial x^2}\right\}\\ \times\exp\left\{-i\Delta t\frac{1}{2\mu_e}\frac{\partial^2}{\partial y^2}\right\}|\Phi'\rangle. \quad \text{(A7)}\end{aligned}$$

In the SAG method, the differentiation along y is rewritten by utilizing the symmetry of the wave function and the kinetic energy operator as

$$\begin{aligned}&\exp\left\{-i\Delta t\frac{1}{2\mu_e}\frac{\partial^2}{\partial y^2}\right\}|\Phi'\rangle\\ &\quad\to P_{xy}Q_{\mathrm{B}}\left[\exp\left\{-i\Delta t\frac{1}{2\mu_e}\frac{\partial^2}{\partial x^2}\right\}|\Phi'\rangle\right]\\ &\quad+Q_{\mathrm{S}}\left[\exp\left\{-i\Delta t\frac{1}{2\mu_e}\frac{\partial^2}{\partial y^2}\right\}|\Phi'\rangle\right], \quad \text{(A8)}\end{aligned}$$

where P_{xy} exchanges x and y, and Q_{B} and Q_{S} extract the wave packets in the domains B and S, respectively. The second term represents the differentiation along y in the domain S.

We note here that we can apply the SAG method to the triplet state by modifying Eq. (A8) as

$$\begin{aligned}&\exp\left\{-i\Delta t\frac{1}{2\mu_e}\frac{\partial^2}{\partial y^2}\right\}|\Phi'\rangle\\ &\quad\to P_{xy}Q_B\left[-\exp\left\{-i\Delta t\frac{1}{2\mu_e}\frac{\partial^2}{\partial x^2}\right\}|\Phi'\rangle\right]\\ &\quad+Q_{\mathrm{S}}\left[\exp\left\{-i\Delta t\frac{1}{2\mu_e}\frac{\partial^2}{\partial y^2}\right\}|\Phi'\rangle\right], \quad \text{(A9)}\end{aligned}$$

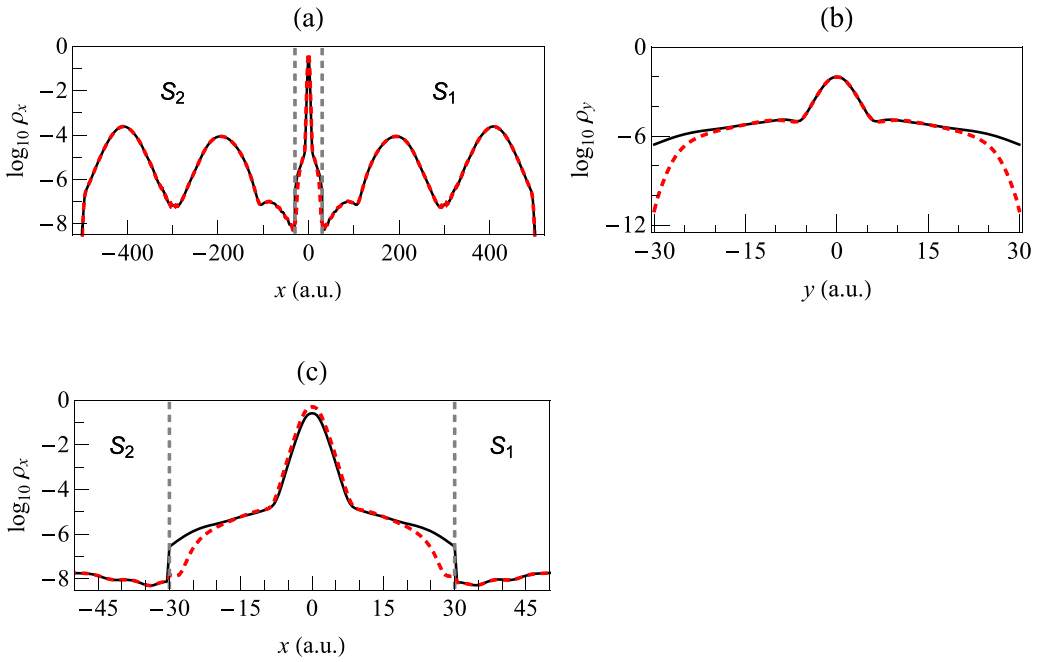

FIG. 5. Spatial distributions of the wave packet along (a) the x direction and (b) the y direction obtained by the SAG method (red dashed curve) and those obtained by the conventional grid method (black solid curve) at the propagation time of 7.257 fs after the interaction with the laser pulse. The enlarged view of (a) is shown in (c). In (a),(c), the boundaries between domain B and domains S_1 and S_2 are indicated by the vertical dashed lines at $x = \pm 30$ a.u.

by taking into account the fact that the spatial wave function of a triplet state is antisymmetric.

In order to examine the accuracy of the SAG method, we performed test calculations with the nuclei fixed at the equilibrium distance of H_2. The electronic ground state of H_2 is obtained by imaginary-time propagation. We stop the wave-packet propagation 7.257 fs after the interaction with the laser pulse (40 nm, 20 cycles, and 1.0×10^{15} W cm^{-2}). The spatial distributions of the wave packet along the x direction, ρ_x, and y direction, ρ_y, defined as

$$\rho_x = \int dy |\Phi(x,y)|^2, \quad \rho_y = \int dx |\Phi(x,y)|^2, \tag{A10}$$

are shown in Fig. 5. In this test calculation, the grid space for the conventional grid method is defined as $|x|, |y| \leqslant 500$ a.u., and for the SAG method as $|x| \leqslant 500$ a.u., $|y| \leqslant 30$ a.u.; i.e., the grid space is reduced by about $500/30 \cong 17$ times. For the longer time propagation, the grid space needs to be enlarged. When the size of the two-dimensional grid space is as $L \times L$, the required memory size is proportional to L in the SAG method while it is proportional to L^2 in the conventional method.

In Figs. 5 and 6, the black curves show the results with the conventional grid method, while the red ones show the results with SAG method. In Fig. 5(a) the relative error is smaller than 2% in the domains S_1 and S_2, where the red and the black curves overlap each other almost completely. In Fig. 6(a), the photoelectron spectra obtained by the Fourier transform of the wave packet in the domains S_1 and S_2 are normalized by their own maxima, where the red and the black curves overlap each other almost completely. There are two peaks at 0.66 and at 0.13 a.u. By comparing the photon energy, 1.139 a.u., with the energy gap between the initial state and $1s\sigma_g$ of H_2^+, 0.482 a.u., and with the energy gap between the initial state and $2p\sigma_u$ of H_2^+, 1.006 a.u., the higher energy peak corresponds to the direct ionization to $1s\sigma_g$ while the lower energy peak corresponds to the ionization to $2p\sigma_u$, which is called a shake-up process. In Fig. 6(b), the difference between the two spectra calculated by subtracting the amplitude obtained by the conventional method from the amplitude obtained by the SAG method is plotted. As shown in this figure, the absolute values of the difference are smaller

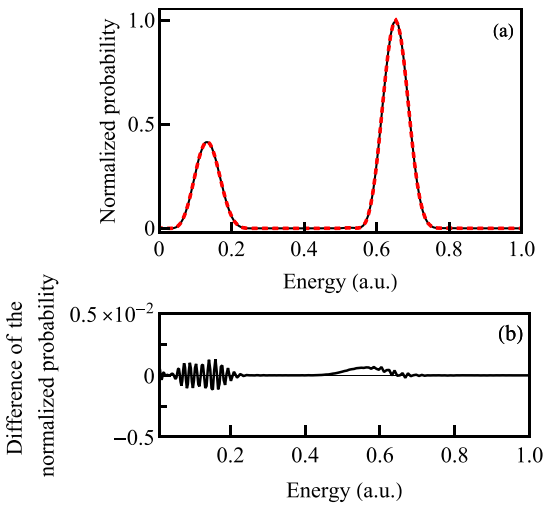

FIG. 6. (a) Photoelectron energy distributions obtained by the SAG method (red dashed curve) and those obtained by the conventional grid method (black solid curve). (b) Magnified difference defined as "the red curve" and "the black curve" in (a).

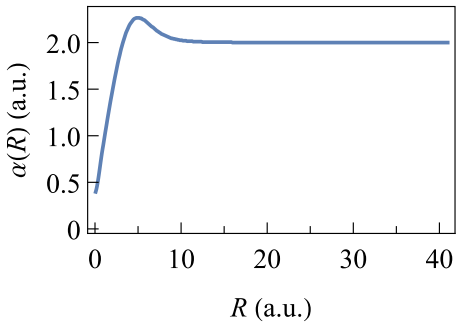

FIG. 7. The softening parameter $\alpha(R)$ in Eq. (18b) as a function of the internuclear distance.

than 0.001 32 even in the photoelectron kinetic energy regions of 0.05–0.30 a.u. and 0.57–0.80 a.u.

As mentioned in the paragraph before Eq. (A3), the wave packet $|\Phi_{S1,S2}(T)\rangle$ has the contribution from the electronically excited states of $H_2{}^+$ like $2p\sigma_u$. However, we eliminate the contribution from such electronic states by projecting $|\Phi_{S1,S2}(T)\rangle$ on the electronic ground state of $H_2{}^+$, by which we can calculate the reduced density matrix of the vibrational states in the electronic ground state.

APPENDIX B: TIME PROPAGATION

We obtain first the initial state by the imaginary-time propagation [45]. As the grid spacing, we adopt $\Delta_x = \Delta_y = 0.50$ a.u. and $\Delta_R = 0.08$ a.u. The grid size is $|x| \leqslant 500$ a.u., $|y| \leqslant 30$ a.u., and 0.08 a.u. $\leqslant R \leqslant 40.96$ a.u. The softening parameter for the electron-nuclear attraction $\alpha(R)$ is shown in Fig. 7 and that for the electron-electron repulsion is $\beta = 0.35$. In the time propagation by the split-operator method, we adopt FFT [46–48]. The time step for the imaginary-time propagation, $\Delta\tau$, is $\Delta\tau = 0.05$ a.u. for $H_2{}^+$ and that for H_2 is $\Delta\tau = 0.10$ a.u. In order to resolve the small energy difference among the vibrationally highly excited states of $H_2{}^+$, we adopt the smaller time step for $H_2{}^+$.

We calculate the energy and the equilibrium internuclear distance of H_2 in the electronic ground state to be $E_0 = -1.036$ a.u. and $R_{\rm eq} = 1.397$ a.u., respectively, which are in good agreement with the reference values of $E_0^{\rm ref.} = -1.165$ a.u. and $R_{\rm eq}^{\rm ref.} = 1.401$ a.u., obtained by solving the time-independent Schrödinger equation with the exact potential energy curve [40].

The functional form of the complex absorbing potential (CAP) is

$$V_{\rm CAP}^{\xi} = \begin{cases} -i\eta_\xi(|\xi| - \xi_{\rm CAP})^2, & |\xi| \geqslant \xi_{\rm CAP} \\ 0, & \text{elsewhere} \end{cases}, \tag{B1}$$

where $\xi = x,\ y$, and R. We adopt $\eta_x = \eta_y = 0.05$, $x_{\rm CAP} = 450$ a.u., $y_{\rm CAP} = 25$ a.u., $\eta_R = 0.01$, and $R_{\rm CAP} = 32.96$ a.u. We consider that a hydrogen molecule in the ground state is exposed to a Fourier-limited laser pulse having a cosine-squared envelope,

$$E(t) = \begin{cases} E_0 \cos^2\left(\frac{\pi}{T_{\rm pulse}} t\right) \cos(\omega t), & |t| \leqslant T_{\rm pulse}/2 \\ 0, & \text{otherwise} \end{cases}, \tag{B2}$$

where $T_{\rm pulse}$ defined as

$$T_{\rm pulse} = N\frac{2\pi}{\omega} \tag{B3}$$

is referred to as the pulse duration and N is the number of optical cycles. The light-field intensity is in the range of $I = 5 \times 10^{12}$–10^{16} W cm^{-2} and the central wavelength of the light field is in the range of $\lambda = 20$–90 nm. The time step is $\Delta t = 0.1$ a.u. After the light field vanishes, the field-free propagation proceeds until certain time T. The reduced density matrix is calculated and renormalized so that $\mathrm{Tr}(\rho_{\rm vib}) = 1$ is satisfied.

[1] P.-O. Löwdin, Phys. Rev. **97**, 1474 (1955).
[2] W. Kohn and L. J. Sham, Phys. Rev. **140**, A1133 (1965).
[3] R. Car and M. Parrinello, Phys. Rev. Lett. **55**, 2471 (1985).
[4] J. C. Tully, J. Chem. Phys. **93**, 1061 (1990).
[5] M. C. Tichy, F. Mintert, and A. Buchleitner, J. Phys. B: At. Mol. Opt. Phys. **44**, 192001 (2011).
[6] E. Schrödinger, Math. Proc. Cambridge Philos. Soc. **31**, 555 (1935).
[7] R. F. Werner, Phys. Rev. A **40**, 4277 (1989).
[8] A. Peres, Phys. Rev. Lett. **77**, 1413 (1996).
[9] M. Horodecki, P. Horodecki, and R. Horodecki, Phys. Lett. A **223**, 1 (1996).
[10] C. H. Bennett, A. W. Harrow, D. W. Leung, and J. A. Smolin, IEEE Trans. Inf. Theory **49**, 1895 (2003).
[11] S. Bäuml, S. Das, and M. M. Wilde, Phys. Rev. Lett. **121**, 250504 (2018).
[12] P. Tommasini, E. Timmermans, and A. F. R. de T. Piza, Am. J. Phys. **66**, 881 (1998).
[13] A. Ekert and P. L. Knight, Am. J. Phys. **63**, 415 (1995).
[14] M. V. Fedorov, M. A. Efremov, A. E. Kazakov, K. W. Chan, C. K. Law, and J. H. Eberly, Phys. Rev. A **69**, 052117 (2004).
[15] S. Majorosi, M. G. Benedict, and A. Czirják, Phys. Rev. A **96**, 043412 (2017).
[16] Z. Huang and S. Kais, Chem. Phys. Lett. **413**, 1 (2005).
[17] Z. Huang, H. Wang, and S. Kais, J. Mod. Opt. **53**, 2543 (2006).
[18] L. K. McKemmish, R. H. McKenzie, N. S. Hush, and J. R. Reimers, J. Chem. Phys. **135**, 244110 (2011).
[19] A. F. Izmaylov and I. Franco, J. Chem. Theory Comput. **13**, 20 (2017).
[20] J. L. Sanz-Vicario, J. F. Pérez-Torres, and G. Moreno-Polo, Phys. Rev. A **96**, 022503 (2017).
[21] Y. Cheng and L. Zhai, J. At. Mol. Sci **7**, 213 (2016).
[22] E. Goulielmakis, Z.-H. Loh, A. Wirth, R. Santra, N. Rohringer, V. S. Yakovlev, S. Zherebtsov, T. Pfeifer, A. M. Azzeer, M. F. Kling, S. R. Leone, and F. Krausz, Nature **466**, 739 (2010).
[23] N. Rohringer and R. Santra, Phys. Rev. A **79**, 053402 (2009).
[24] S. Carlström, J. Mauritsson, K. J. Schafer, A. L'Huillier, and M. Gisselbrecht, J. Phys. B: At. Mol. Opt. Phys. **51**, 015201 (2018).
[25] M. Vatasescu, Phys. Rev. A **88**, 063415 (2013).
[26] M. Vatasescu, Phys. Rev. A **92**, 042323 (2015).

[27] J. Schliemann, J. I. Cirac, M. Kuś, M. Lewenstein, and D. Loss, Phys. Rev. A **64**, 022303 (2001).
[28] G. C. Ghirardi and L. Marinatto, Fortschr. Phys. **51**, 379 (2003).
[29] G. C. Ghirardi and L. Marinatto, Phys. Rev. A **70**, 012109 (2004).
[30] P. Zanardi, Phys. Rev. Lett. **87**, 077901 (2001).
[31] F. Herbut and M. Vujičić, J. Phys. A: Math. Gen. **20**, 5555 (1987).
[32] F. Herbut, Am. J. Phys. **69**, 207 (2001).
[33] T. Sasaki, T. Ichikawa, and I. Tsutsui, Phys. Rev. A **83**, 012113 (2011).
[34] V. Vedral and M. B. Plenio, Phys. Rev. A **57**, 1619 (1998).
[35] G. Vidal, J. Mod. Opt. **47**, 355 (2000).
[36] G. Jaeger, *Quantum Information* (Springer, New York, 2007).
[37] C. H. Bennett, H. J. Bernstein, S. Popescu, and B. Schumacher, Phys. Rev. A **53**, 2046 (1996).
[38] S. Luo, Phys. Rev. A **77**, 022301 (2008).
[39] M. Lein, T. Kreibich, E. K. U. Gross, and V. Engel, Phys. Rev. A **65**, 033403 (2002).
[40] T. E. Sharp, At. Data Nucl. Data Tables **2**, 119 (1970).
[41] Y. Nabekawa, Y. Furukawa, T. Okino, A. A. Eilanlou, E. J. Takahashi, K. Yamanouchi, and K. Midorikawa, Sci. Rep. **5**, 11366 (2015).
[42] Y. Nabekawa, Y. Furukawa, T. Okino, A. A. Eilanlou, E. J. Takahashi, K. Yamanouchi, and K. Midorikawa, Nat. Commun. **6**, 8197 (2015).
[43] J. Rapp and D. Bauer, Phys. Rev. A **89**, 033401 (2014).
[44] R. Kosloff and D. Kosloff, J. Comput. Phys. **63**, 363 (1986).
[45] R. Kosloff and H. Tal-Ezer, Chem. Phys. Lett. **127**, 223 (1986).
[46] J. A. Fleck, J. R. Morris, and M. D. Feit, Appl. Phys. **10**, 129 (1976).
[47] M. D. Feit, J. A. Fleck, and A. Steiger, J. Comput. Phys. **47**, 412 (1982).
[48] D. Kosloff and R. Kosloff, J. Comput. Phys. **52**, 35 (1983).